Physica Medica xxx (2014) 1–8

Contents lists available at ScienceDirect

Physica Medica

journal homepage: http://www.physicamedica.com

Original paper

Resolution-recovery-embedded image reconstruction for a high-resolution animal SPECT system

Navid Zeraatkar [a], Salar Sajedi [a], Mohammad Hossein Farahani [a, b], Hossein Arabi [a, b], Saeed Sarkar [a, c], Pardis Ghafarian [d, e], Arman Rahmim [f, g], Mohammad Reza Ay [a, c, *]

[a] Research Center for Molecular and Cellular Imaging, Tehran University of Medical Sciences, Tehran, Iran
[b] Parto Negar Persia Co, Tehran, Iran
[c] Department of Medical Physics and Biomedical Engineering, Tehran University of Medical Sciences, Tehran, Iran
[d] Chronic Respiratory Diseases Research Center, National Research Institute of Tuberculosis and Lung Diseases (NRITLD), Shahid Beheshti University of Medical Sciences, Tehran, Iran
[e] PET/CT and Cyclotron Center, Masih Daneshvari Hospital, Shahid Beheshti University of Medical Sciences, Tehran, Iran
[f] Department of Radiology, Johns Hopkins University, Baltimore, MD, USA
[g] Department of Electrical and Computer Engineering, Johns Hopkins University, Baltimore, MD, USA

ARTICLE INFO

Article history:
Received 2 September 2013
Received in revised form
29 May 2014
Accepted 30 May 2014
Available online xxx

Keywords:
Small-animal
SPECT
HiReSPECT
Resolution recovery
H8500
Parallel-hole

ABSTRACT

The small-animal High-Resolution SPECT (HiReSPECT) is a dedicated dual-head gamma camera recently designed and developed in our laboratory for imaging of murine models. Each detector is composed of an array of 1.2 × 1.2 mm^2 (pitch) pixelated CsI(Na) crystals. Two position-sensitive photomultiplier tubes (H8500) are coupled to each head's crystal. In this paper, we report on a resolution-recovery-embedded image reconstruction code applicable to the system and present the experimental results achieved using different phantoms and mouse scans. Collimator-detector response functions (CDRFs) were measured via a pixel-driven method using capillary sources at finite distances from the head within the field of view (FOV). CDRFs were then fitted by independent Gaussian functions. Thereafter, linear interpolations were applied to the standard deviation (σ) values of the fitted Gaussians, yielding a continuous map of CDRF at varying distances from the head. A rotation-based maximum-likelihood expectation maximization (MLEM) method was used for reconstruction. A fast rotation algorithm was developed to rotate the image matrix according to the desired angle by means of pre-generated rotation maps. The experiments demonstrated improved resolution utilizing our resolution-recovery-embedded image reconstruction. While the full-width at half-maximum (FWHM) radial and tangential resolution measurements of the system were over 2 mm in nearly all positions within the FOV without resolution recovery, reaching around 2.5 mm in some locations, they fell below 1.8 mm everywhere within the FOV using the resolution-recovery algorithm. The noise performance of the system was also acceptable; the standard deviation of the average counts per voxel in the reconstructed images was 6.6% and 8.3% without and with resolution recovery, respectively.

Introduction

Recently, application of small-animal models in the context of *in-vivo* biomedical research has been increasing significantly [1,2]. This has led to a need for dedicated small-animal imaging systems to provide enhanced spatial resolution and sensitivity [3–8]. As a result, there are ongoing advancements in both instrumentation and image reconstruction for small-animal single-photon emission computed tomography (SPECT) [9].

Image reconstruction algorithms are divided into two main categories: analytic and iterative methods [10,11]. Although analytical methods of tomographic image reconstruction, in particular, filtered backprojection (FBP), continue to be used, their inherent disadvantages such as noise enhancement and streak artifacts have led to the emergence of iterative reconstruction algorithms. Such iterative methods can incorporate, in the reconstruction process, modeling of and correction for physical factors which degrade image quality and

* Corresponding author. Department of Medical Physics and Biomedical Engineering, Tehran University of Medical Sciences, Tehran, Iran. Tel./fax: +98 21 66907532.
E-mail address: mohammadreza_ay@sina.tums.ac.ir (M.R. Ay).

http://dx.doi.org/10.1016/j.ejmp.2014.05.013
1120-1797/

quantitative accuracy. These factors include scatter, attenuation, and detector response. Iterative methods, in particular, the commonly used maximum-likelihood expectation-maximization (MLEM) (and its accelerated version, ordered-subsets expectation-maximization (OSEM)), have been demonstrated improved lesion detectability, even under low-count conditions, compared to FBP [12–14].

In small-animal imaging, excellent spatial resolution is particularly critical because of the small sizes of organs and tumors in rodent models. Nonetheless, the collimator-detector response (CDR) [15,16], reflected as the finite dispersion (or blurring) of the detected counts emanating from a point source of activity, remains one of the principal factors limiting spatial resolution in SPECT. Consequently, a great deal of effort has been devoted to develop methods for modeling of and compensation for CDR [17–19]. Iterative reconstruction algorithms enable inclusion of CDR compensation. This may be achieved by defining a projector–backprojector pair that includes CDR function (CDRF) modeling, which can be performed using either ray-driven or pixel-driven methods. The main difference between these two methods is that in pixel-driven methods modeling is performed by tracing the projection bins from the image matrix pixels toward the projection bins, while ray-driven techniques propagate the rays from projection bins towards the image matrix [15,20].

A High-Resolution SPECT (HiReSPECT) scanner for small-animal imaging has been recently designed and developed in the Research Center for Molecular and Cellular Imaging, Institute for Advanced Medical Technologies, Tehran University of Medical Sciences, Iran [21]. We present in this work an MLEM-based resolution recovery algorithm, applying rotation-based methods [22,23] to both accelerate the code and also for ease of CDRF compensation. Next, we introduce the dedicated algorithm we developed for resolution-recovery-embedded image reconstruction of the HiReSPECT data and present various evaluation results.

Materials and methods

The system specifications

The HiReSPECT scanner, in its current version, consists of two imaging detectors (Fig. 1). Though the heads have been designed such that different collimator types can be installed, parallel-hole collimators have been used in the current version. Both heads can translate synchronously in the radial direction to alter the radius of rotation (RoR). Moreover, the system has a table (bed) with a long-range translational movement for the object being scanned (phantom or animal) (Fig. 1). The entire gantry can rotate around the object in order to acquire 2-dimensional (2D) projections. Both collimators are composed of lead with hexagonal holes. The aperture width of the holes, the septa width and the thickness of the collimator are 1.2 mm, 0.2 mm, and 34 mm, respectively. Pixelated sodium-doped cesium iodide (CsI(Na)) scintillator crystals were utilized. The pixel area is 1×1 mm^2 with an inter-pixel separation of 0.2 mm, resulting in a pitch of 1.2 mm. The crystal is comprised of an array of 46×89 pixels. The thickness of the crystal is 5 mm. For each head, the crystal is coupled to two H8500 position-sensitive photomultiplier tubes (PS-PMTs) (Hamamatsu Photonics, Japan). More details can be found in our recent publication [21].

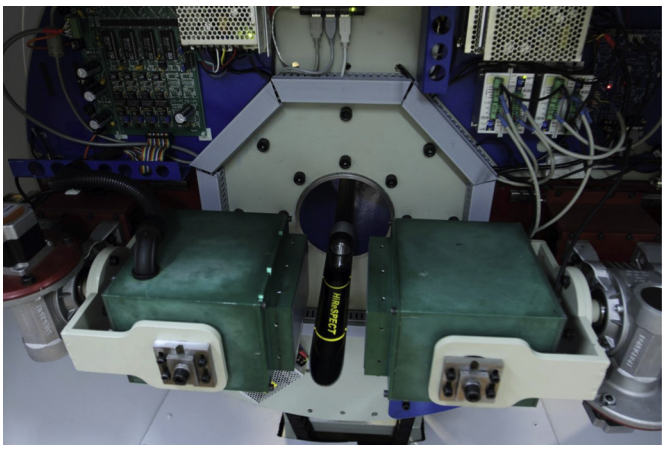

Figure 1. A close-up view of the HiReSPECT gantry.

Characterizing the CDRF

The pixel-driven approach was pursued for resolution recovery (more information provided in *Section 1*), and we therefore needed to characterize the set of CDRFs for all pixels in the FOV. However, considering that the CDRF is nearly uniform for all pixels in planes parallel to the collimator face (with the exception of pixels corresponding to marginal areas of the collimator), we characterized the CDRF specific to each plane.

The projection matrix of the readout module has dimensions of 38×80. However, we used a 3-dimensional (3D) image matrix size of $114 \times 114 \times 240$ for the reconstruction leading to voxel sizes of $(0.3\ \text{mm})^3$. This included 240 planes along the 'z' direction (parallel to the 'x–y' plane), while having 114 planes parallel to the collimator face. Instead of performing an independent measurement for every distance from the head corresponding to each of the aforementioned 114 planes, we first obtained the CDRFs for a number of distances from the head and then, using interpolation, we expanded it to the other distances.

To measure the CDRFs, we filled a glass capillary source having an internal diameter of ~1.1 mm with 0.5 mCi of ^{99m}Tc. Then, we placed it parallel to the head at three different distances of 5, 25, and 50 mm, once along the long dimension and then along the perpendicular dimension through 6 independent measurements. Three one-dimensional (1D) count profiles perpendicular to the capillary were selected from the planar images thus obtained in every plane and were fitted to a Gaussian function, producing standard deviations along the x (σ_x) and y (σ_y) directions depending on the orientation of the rod. The three resulting values for a given distance and orientation were then averaged.

Having σ_x and σ_y for the measured distances from the head, we performed linear interpolation to estimate σ_x and σ_y for any given distance from the head (Sec 3.1). The assumption of linearity is valid for typical imaging distances from the head (as seen in Ref. [15]: Eq (6) and Fig. 3 in that reference), justifying the proposed approach. The CDRF at every distance was then defined by its σ_x and σ_y via a 2D Gaussian equation as:

$$f(x,y) = Ae^{-\left(\frac{(x-x_0)^2}{2\sigma_x^2}+\frac{(y-y_0)^2}{2\sigma_y^2}\right)} \quad (1)$$

where x_0 and y_0 are the means along the x and y directions, respectively. Furthermore, A is the amplitude of f at the point (0,0).

Dedicated rotation method

In SPECT imaging, the head rotates around the object. However, rotation-based reconstruction algorithms are based on the assumption that the head is fixed and the object (image matrix) rotates [15]. This assumption can ease the process of CDRF compensation in iterative image reconstruction algorithms and

Please cite this article in press as: Zeraatkar N, et al., Resolution-recovery-embedded image reconstruction for a high-resolution animal SPECT system, Physica Medica (2014), http://dx.doi.org/10.1016/j.ejmp.2014.05.013

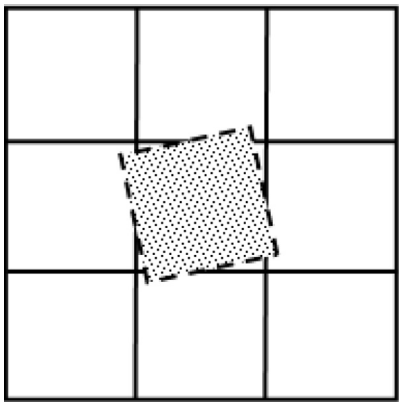

Figure 2. Since we used 78° jumps in the reconstruction code, supposing that the head is fixed and the object (image matrix) rotates (based on the rotation-based algorithm), the mentioned 78° jumps in reality translates to −78° rotation in the image matrix domain. As an example, a 1 × 1 source matrix (showed by dashed pixel) only corresponds to 5 pixels of a 9 × 9 target matrix (showed by solid pixels) by a −78° rotation. The fraction of the source pixel assigned to each of the mentioned 5 pixels can be stored in a LUT. In a similar way, having a pre-calculated LUT and the value of the 5 pixels, the value of the source matrix can be calculated.

accelerate the reconstruction code. A number of algorithms can be utilized in the context of rotation-based iterative reconstruction. Di Bella et al. compared some of them in terms of efficiency and accuracy [24]. To enable accurate and at the same time efficient implementation, we developed our own rotation algorithm on a C++ platform. The rotating matrix of the source is designated the "source matrix" and the resulting image matrix the "target matrix," rotating the source matrix an angle θ from a starting position of 0°. We first calculated the Cartesian coordinates of the pixel centers in the source matrix with respect to the known coordinates of the pixel centers of the target matrix.

In the case of a 78° rotation (which is used in our algorithm and will be explained in the next section), each source pixel corresponds to a maximum number of 5 target pixels, and vice versa. Figure 2 demonstrates this for 9 target-image pixels (solid lines) and one source-matrix pixel (dashed lines), where the latter intersects only 5 (out of 9 total) voxels. In our technique, the corresponding 5 pixels of the target for each source pixel and the fraction of counts that should be assigned to each of those 5 pixels are computed analytically for θ of −78°. The data calculated in this way, which are needed for rotating a source matrix, can be stored once as small-size look-up tables (LUTs), which are subsequently loaded when required.

Our dedicated fixed-angle rotation algorithm is computationally more efficient than the classical implementation of bilinear rotation. This is because in rotating an $N \times N$ matrix using bilinear rotation, $N \times N \times 8$ multiplications are needed (for each pixel, 4 multiplications are needed to compute the rotated x and y coordinates and 4 for bilinear interpolation). By contrast, our code requires $N \times N \times 5$ multiplications utilizing the pre-generated LUTs. This means a factor of at least 8/5 acceleration in rotation.

In order to evaluate our reconstruction algorithm, we compared it with bilinear interpolation using the 2D Shepp–Logan phantom [25]. For this, a 128 × 128 Shepp–Logan phantom image (Fig. 3a) was rotated by our algorithm and the standard bilinear algorithm performing total rotation of 4680° using 60 steps in a way that each step applied a 78° rotation. Rotating the image 60 times (78° each time) makes it return to the original angle (4680° = 13 × 360°), while covering all 6° increments. This provided us with a good comparison tool. For this, we used the Normalized Square Error (NSE) according to the equation below to assess the performance of our rotation algorithm using the original image as the reference image:

$$\mathrm{NSE} = \frac{\sum_{n=1}^{N} (\mathrm{Rot}(n) - \mathrm{Ref}(n))^2}{\sum_{n=1}^{N} (\mathrm{Ref}(n))^2} \quad (2)$$

where *Rot*, *Ref*, *n*, and *N* denote the 60-times rotated matrix, the reference matrix, the pixel index number, and the number of pixels in the matrix (i.e. 128 × 128 = 16,384), respectively.

The dedicated resolution recovery-embedded image reconstruction code

We developed a dedicated code for resolution recovery and image reconstruction for the HiReSPECT scanner. We combined a modified MLEM algorithm with a pixel-driven rotation-based resolution recovery technique. Hereafter, we further elaborate upon the reconstruction algorithm.

The CDRFs corresponding to the 114 planes parallel to the collimator are obtained using the abovementioned formulas. This is done prior to the start of each iteration in order to minimize the time required within the loops of the code. The RoR at which data acquisition has been performed is imported into the code to correctly define the CDRFs. A set of images of uniform discs corresponding to the FOV (including the total acquired counts) is considered as the initial "estimate." As previously mentioned, the 3D image matrix size is 114 × 114 × 240, and the entire process is performed in three dimensions using the acquired projection views (PVs). Sub-iterations (every iteration has sub-iterations equal to the number of PVs) start after the initial estimate is calculated. Supposing that *n_views* PVs are acquired in 360°, each iteration includes *n_views* sub-iterations. The first subroutine in every sub-iteration is forward projection (FP). For this, according to the rotation-based method, the entire 3D image matrix is rotated through an angle equal to the corresponding angle of the PV. The pre-generated rotation maps using the rotation algorithm described in Section 2.3 are applied in the code. After the rotation is performed, every plane in the image matrix parallel to the collimator face is convolved in two dimensions with the CDRF

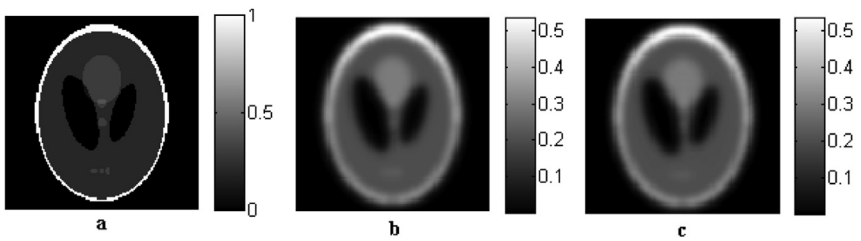

Figure 3. (a) The original Shepp-Logan phantom image, (b) the 60-time rotated image using bilinear rotation, and (c) the 60-time rotated image using our pre-generated LUTs rotation (c).

Please cite this article in press as: Zeraatkar N, et al., Resolution-recovery-embedded image reconstruction for a high-resolution animal SPECT system, Physica Medica (2014), http://dx.doi.org/10.1016/j.ejmp.2014.05.013

corresponding to the distance of the plane from the collimator. Following the convolution stage, the FP process is performed. In the current case in which the image matrix is parallel to the head, performing FP is straightforward. Thereafter, the PV matrix resulted from FP (the FP-PV matrix) is used for determination of the difference between the estimated solution (FP-PV) and the measured PV. The measured PV matrix is divided pixel-by-pixel by the FP-PV matrix and the result is stored in a new matrix (ratio matrix) having the same dimensions as the PV matrix. In order to compensate for the difference, the ratio matrix should be transformed from the projection domain to the image domain; this requires back-projection (BP).

The ratio matrix is back-projected onto the rotated image matrix. In the BP procedure, in a similar way to what was done in the case of FP, every plane parallel to the head is convolved with the corresponding CDRF. In other words, the overall forward projection including CDRF compensation matches the back projection operator, which provides improved convergence compared to the use of mismatched projectors [26]. Furthermore, we note that because the CDRF is symmetric, forward and back-projection operations both involve convolutions with the same function.

Subsequently, the updated image matrix is created. The updated image matrix would be used as the initial estimate of the next sub-iteration (or the next iteration). We also employed another modification in our code to enhance convergence. In the MLEM algorithm, one may ordinarily pass through views sequentially across the updates, but this can result in slow convergence. Our default acquisition protocol is 60 views over 360° with angular view-to-view steps of 6°. We use a 13-step jump (equivalent to 78° because every step corresponds to 6°) for the next sub-iteration in every iteration. In this manner, the convergence becomes faster. The number of iterations should be selected to reach the desired image quality.

Phantom studies

A capillary source was utilized to assess the spatial resolution of the system following different image reconstructions. For this, a glass capillary with an internal diameter of ~1.1 mm and external diameter of 1.5 mm was filled with a solution of normal saline and ^{99m}Tc with the activity of 0.5 mCi. Data acquisition was performed in 60 views over 360° while time per view was compensated for decay (the default acquisition protocol). Acquisition time for the first view was adjusted to 60 s. At the same time, we explored usage of a decay-adjusted data acquisition capability in our system wherein the acquisition time for each view exceeded that of the previous view to accommodate this effect. The capillary source was located at the axis of rotation. Data were then reconstructed using 2 iterations with and without resolution recovery.

In addition, a combination of 5 capillary sources was scanned with the default acquisition protocol. The distance between each two neighboring capillaries was 9 mm. Each capillary was filled with 200 μCi of Tc-99m at the start of scan. The acquisition time was set to 120 s for the first view while decay-adjusted acquisition was also enabled.

A specially fabricated 'Jaszczak-like' phantom was used to evaluate overall image quality using the various reconstruction approaches. The main part of the phantom is a cylinder 35 mm in height and 32 mm in diameter. Inside it, various fillable rods were drilled in 6 sections. The radii of rods range from 1.6 to 2.8 mm with steps of 0.2 mm from section to section. In each section, the distance between adjacent rods is equal to the radius of the rods in that section. For data acquisition, the phantom was filled with 2 mCi of Tc-99m in a uniform normal saline solution and the default acquisition protocol used. Acquisition time for the first view was adjusted to 60 s. The decay compensation option, as described previously, was enabled in the acquisition program. The data were then reconstructed using 2 full iterations by two options: first disabling the resolution recovery option and then enabling it. No smoothing filter was applied to the projection or the reconstructed data.

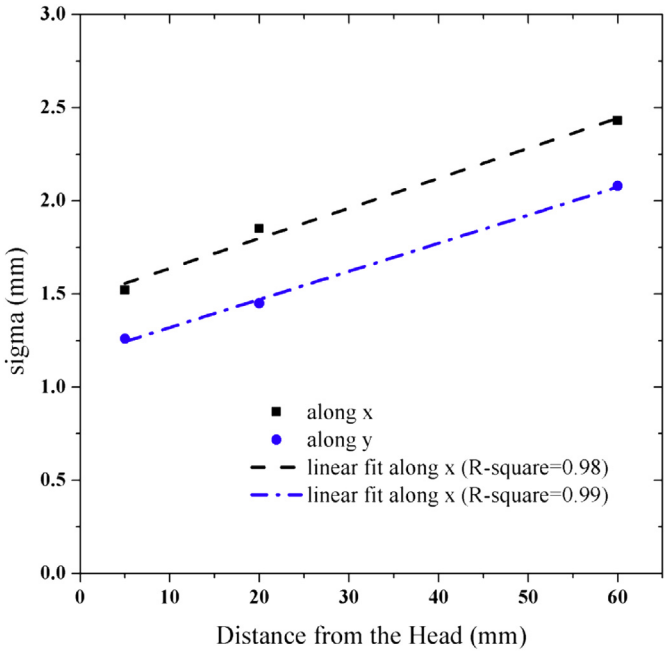

Figure 4. Measured values of σ_x and σ_y that are used in estimating the CDRF by 2D Gaussian functions together with the lines fitted to them for calculating σ_x and σ_y corresponding to any other non-measured distance from the head.

Finally, in order to evaluate the noise characteristics and uniformity performance of the HiReSPECT, a NEMA NU-4 [27] image quality phantom was used. The phantom was filled with 5 mCi of Tc-99m. Data acquisition was performed using the default protocol with an acquisition time of 120 s for the first view and decay-compensated acquisition enabled. Image reconstruction was then performed using 5 iterations with and without resolution recovery. A 22.5 mm-diameter by 10 mm-long cylindrical volume of interest (VOI) was selected over the center of the uniform part of the phantom. The percentage standard deviation (%STD) in this VOI was then measured [27].

Whole-body animal scans

Whole-body mouse studies were performed using ^{99m}Tc-Methylene Diphosphonate (MDP) for skeletal scanning and also ^{99m}Tc-Dimercapto Succinic Acid (DMSA) for renal scintigraphy. Two mCi were injected into the mouse in each study, and data were acquired using the default acquisition protocol. Data acquisition time for the first view was 60 s. The mice were placed under general anesthesia during the scans. The data were then reconstructed using 2 full iterations without and with resolution recovery.

Results

Obtaining CDRF

The parameters $\sigma_x(d)$ and $\sigma_y(d)$ were parameterized as functions of the distance d from the collimator via linear interpolation, enabling generation of CDRFs for any desired distance from the

Please cite this article in press as: Zeraatkar N, et al., Resolution-recovery-embedded image reconstruction for a high-resolution animal SPECT system, Physica Medica (2014), http://dx.doi.org/10.1016/j.ejmp.2014.05.013

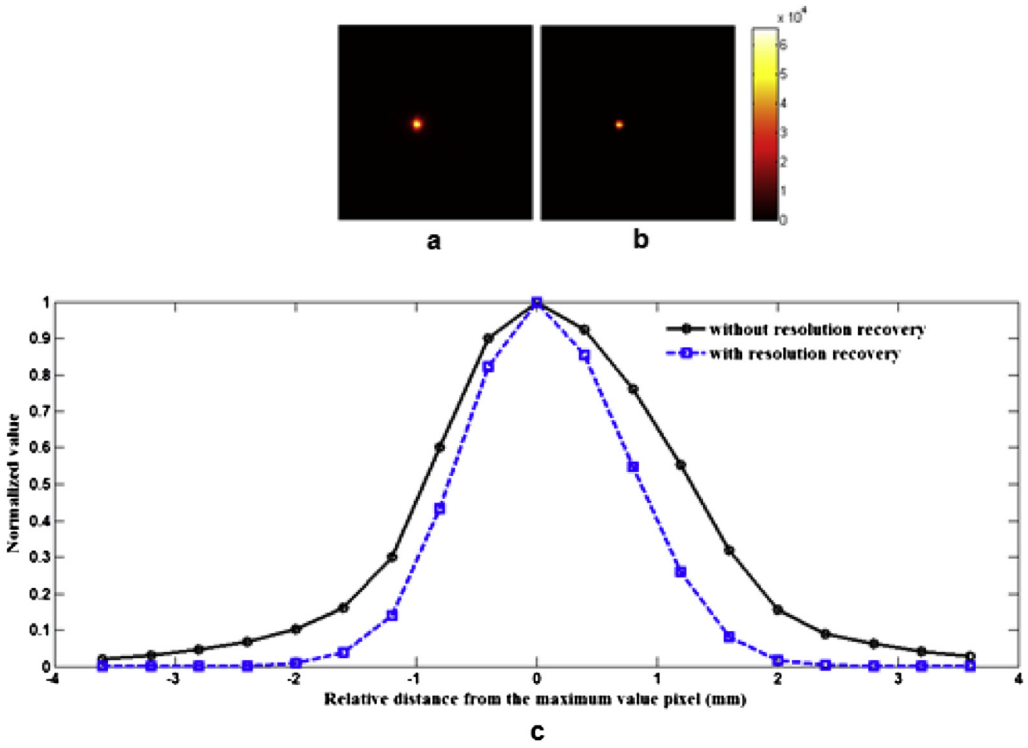

Figure 5. The transverse reconstructed images of the single capillary source after 2 iterations (a) without and (b) with resolution recovery, together with (c) the illustration of radial resolution measured at the position of the single capillary source in terms of FWHM with and without resolution recovery.

collimator. Eq (3) and Eq (4) express the resulting terms for $\sigma_x(d)$ and $\sigma_y(d)$ which are also shown in Fig. 4 together with the original measured values.

$$\sigma_x(d) = 0.016d + 1.48mm \quad (3)$$

$$\sigma_y(d) = 0.015d + 1.17\ mm \quad (4)$$

In the above equations, $\sigma_x(d)$, $\sigma_y(d)$, and d are in mm.

Evaluation of the rotation method

The calculations demonstrated that the NSE values as measures of rotation accuracy obtained using our rotation algorithm involving pre-generated LUTs versus bilinear rotation are 0.3740 and 0.3738, respectively, demonstrating virtually identical performance. Furthermore, Fig. 3b and c depict the results of 4680° rotations using 60 steps (each step was equal to 78° rotation) via the bilinear rotation method versus rotation technique using pre-generated LUTs. Similar to quantitative NSE value comparisons provided earlier, the two images show no visual discrepancy.

Phantom studies

Figure 5a and b depict the reconstructed transverse images of the single capillary source after 2 iterations without and with resolution recovery, respectively. Meanwhile, 1D count profiles of the mentioned images are shown in Fig. 5c demonstrating the better spatial resolution using resolution recovery. To quantitatively demonstrate the improvement in spatial resolution with resolution

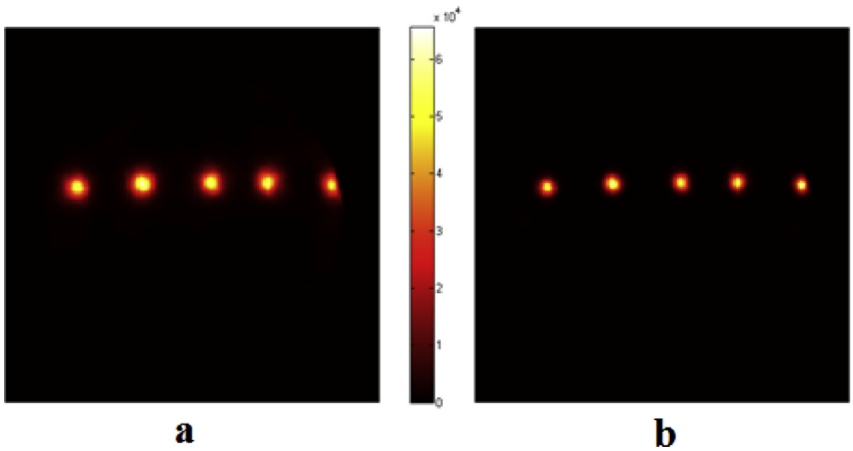

Figure 6. The transverse reconstructed images of the 5 capillaries after 2 iterations (b) without and (c) with resolution recovery.

Please cite this article in press as: Zeraatkar N, et al., Resolution-recovery-embedded image reconstruction for a high-resolution animal SPECT system, Physica Medica (2014), http://dx.doi.org/10.1016/j.ejmp.2014.05.013

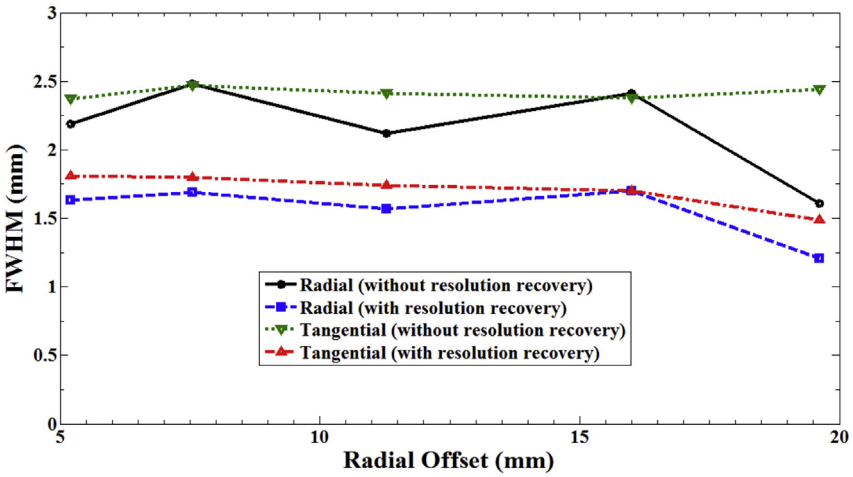

Figure 7. Radial and tangential spatial resolution (FWHM) as a function of radial offset.

recovery, 1D count profiles across the reconstructed images of the capillary sources were fit to a Gaussian function and the corresponding FWHM calculated. Our calculations show that FWHM in the radial direction is 2.1 mm without resolution recovery and 1.6 mm with resolution recovery. In the tangential direction, FWHM is 2.2 mm without resolution recovery and 1.6 mm with resolution recovery.

The transverse reconstructed images of the 5 capillary sources are depicted in Fig. 6a and b. Figure 6a shows the resultant image after 2 iterations without resolution recovery, and Fig. 6b demonstrates the outcome image after the same number of iterations with resolution recovery. In addition, the spatial resolution was measured in terms of FWHM along the radial and tangential directions according to the method described for the single capillary. The results (Fig. 7) demonstrate the impact of resolution recovery, improving the FWHM resolution between 0.4 and 0.8 mm in the radial direction and ~0.7 mm in the tangential direction.

The transverse reconstructed image of the Jaszczak-like phantom reconstructed without resolution recovery is shown in Fig. 8a; Fig. 8b depicts the same slice of the phantom reconstructed using resolution recovery. Improved visualization of the rods with resolution recovery is most apparent in the sections with the 1.6- and 1.8-mm rods.

For the NEMA NU-4 image quality phantom, a VOI was selected as described in *Section 2.5*, and the percent standard deviation (STD) were calculated. The results showed that the %STD without and with resolution recovery was 6.6% and 8.3%, respectively.

Whole-body animal scans

The reconstructed images of whole-body scans of a mouse using MDP without and with resolution recovery are shown in Fig. 9a and b, respectively. Similarly, Fig. 9c and d depict the reconstructed images of whole-body scans using DMSA without and with resolution recovery, respectively. The images shown represent maximum intensity projection (MIP) coronal views of the respective animals. No smoothing was applied to the projections or the reconstructed images. Visual comparison of the resulting scan images in Fig. 9 without and with resolution recovery shows the general improvement of the images with resolution recovery in the MDP bone scan and the DMSA renal scan; for example, the skeleton is better defined on the MDP scan and the kidneys better defined on the DMSA scan.

Discussion and conclusion

Assessing all possible positions within the FOV for modeling the CDRF is a time-consuming process whether using experimental methods or by Monte Carlo simulations. Our approach was instead to use the assumption that CDRF is constant within planes parallel to the head in the FOV (neglecting the marginal regions). In addition, we utilized interpolation to generate the CDRF of planes between those characterized using direct measurements. It was demonstrated that this efficient approach resulted in notable resolution enhancements in the reconstructed images.

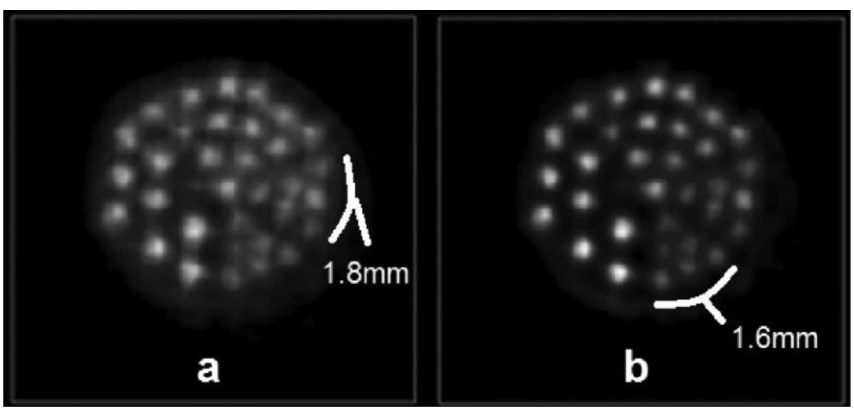

Figure 8. The transverse reconstructed images of the Jaszczak-like phantom after 2 iterations (a) without and (b) with resolution recovery.

Please cite this article in press as: Zeraatkar N, et al., Resolution-recovery-embedded image reconstruction for a high-resolution animal SPECT system, Physica Medica (2014), http://dx.doi.org/10.1016/j.ejmp.2014.05.013

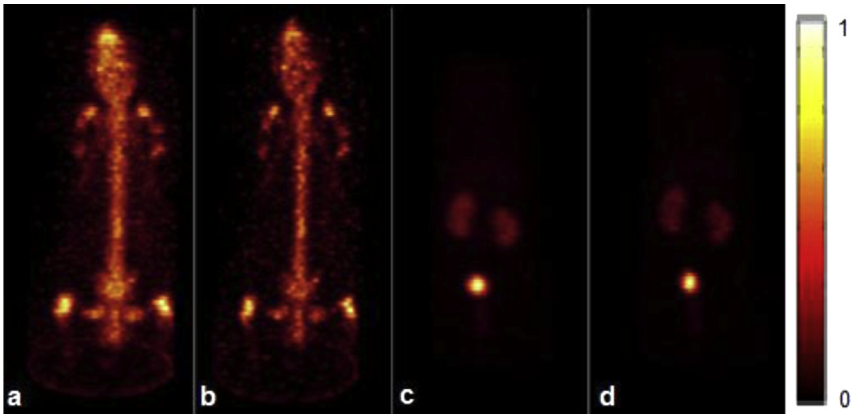

Figure 9. Three-dimensional renderings of the ^{99m}Tc-MDP scans reconstructed (a) without and (b) with resolution recovery. Three-dimensional renderings of the ^{99m}Tc-DMSA scans reconstructed (c) without and (d) with resolution recovery. The images are normalized to their maximum pixel value.

We used a rotation-based method for image reconstruction. This resulted in feasible image reconstructions, also simplifying application of CDRF compensation. In the context of this approach, the 3D image matrix is always divided into planes parallel to the head. Assuming that the CDRF is constant in planes parallel to the head, CDRF is incorporated within the image reconstruction task, including 2D convolutions with the corresponding CDRF at each plane.

In contrast to conventional matrix-rotation algorithms, where rotation is followed by interpolation, our algorithm uses previously generated rotation maps, thereby accelerating projection-image processing and reconstruction. Nevertheless, storing and loading CDRFs in the form of LUTs was not appropriate for two principal reasons: first, a large amount of memory was occupied for saving and loading; secondly, statistical noise diminished the quality and uniformity of the CDRFs leading to low-quality CDRF compensation. Therefore, instead of using raw CDRFs, we fitted every CDRF to a 2D Gaussian function and used the Gaussian function during the reconstruction. This was done in order to (i) make saving and regenerating (loading) of the CDRFs easier using only two values of σ_x and σ_y for every distance and (ii) suppress the effect of statistical noise. Figure 4 illustrates the values of σ_x and σ_y for the measured distances together with the resulting linear regression of σ_x and σ_y versus distance.

The combination of the dedicated rotation algorithm and modified MLEM led to fast convergence in our code. Figure 5c shows that application of resolution recovery improves spatial resolution quantitatively as well; the spatial resolution in terms of tangential and radial FWHM decreased from about 2.2 mm to 1.6 mm.

Based on Fig. 7, it can be concluded that an advantage of applying resolution recovery is to achieve resolution uniformity across the FOV. However, even in this case, resolution tends to improve toward the edges of the FOV. The experiments conducted to assess noise performance for the system showed satisfactory results. However, the enhanced resolution performance was obtained at the cost of somewhat increased noise in the reconstructed images. The implications of the resolution versus noise trade-off in the context of resolution recovery are complex, and should be appropriately studied for specific tasks in SPECT or PET imaging [28–30]. Furthermore, resolution recovery also can produce ringing (Gibbs artifacts), which again is an issue that needs to be better understood and appropriately addressed [28]. Finally, whole-body scans of mice performed using MDP and DMSA and resolution recovery yielded reasonably satisfactory images (Fig. 9).

All scans in the present study were performed using a single-head protocol because the second head was in the process of further calibrations. We presently aim to pursue additional studies using dual-head acquisition and reconstruction. This should not affect the system performance though it will enable shortening the acquisition time at the same count statistics or doubling count statistics using the same acquisition time. In addition, we presently aim to enhance image quality and quantitative accuracy by incorporating attenuation correction within the reconstructions.

Acknowledgments

This work was supported by Tehran University of Medical Sciences under grant 22986.

References

[1] Pomper MG, Lee JS. Small animal imaging in drug development. Curr Pharm Des 2005;11:3247–72.
[2] Peremans K, Cornelissen B, Van Den Bossche B, Audenaert K, Van de Wiele C. A review of small animal imaging planar and pinhole spect gamma camera imaging. Vet Radiol Ultrasound 2005;46(2):162–70.
[3] Beekman FJ, Vastenhouw B. Design and simulation of a high-resolution stationary SPECT system for small animals. Phys Med Biol 2004;49(19):4579–92.
[4] Loudos GK, Nikita KS, Giokaris ND, Styliaris E, Archimandritis SC, Varvarigou AD, et al. A 3D high-resolution gamma camera for radiopharmaceutical studies with small animals. Appl Radiat Isot 2003;58(4):501–8.
[5] Meikle SR, Beekman FJ, Rose SE. Complementary molecular imaging technologies: high resolution SPECT, PET and MRI. Drug Discov Today Technol 2006;3(2):187–94.
[6] Loudos G, Majewski S, Wojcik R, Weisenberger A, Sakellios N, Nikita K, et al. Performance evaluation of a dedicated camera suitable for dynamic radiopharmaceuticals evaluation in small animals. IEEE Trans Nucl Sci 2007;54(3):454–60.
[7] Qian JG, Bradley EL, Majewski S, Popov V, Saha MS, Smith MF, et al. A small-animal imaging system capable of multipinhole circular/helical SPECT and parallel-hole SPECT. Nucl Instrum Meth A 2008;594(1):102–10.
[8] Mitchell GS, Cherry SR. A high-sensitivity small animal SPECT system. Phys Med biology 2009;54(5):1291–305.
[9] Lewitt RM, Matej S. Overview of methods for image reconstruction from projections in emission computed tomography. P IEEE 2003;91(10):1588–611.
[10] Tsui BMW, Frey EC. Analytic image reconstruction methods in emission computed tomography. In: Zaidi H, editor. Quantitative analysis in nuclear medicine imaging. Singapore: Springer; 2006. pp. 82–106.
[11] Hutton BF, Nuyts J, Zaidi H. Iterative reconstruction methods. In: Zaidi H, editor. Quantitative analysis in nuclear medicine imaging. Singapore: Springer; 2006. pp. 107–40.
[12] Shepp LA, Vardi Y. Maximum likelihood reconstruction for emission tomography. IEEE Trans Med Imaging 1982;1(2):113–22.
[13] Dempster AP, Laird NM, Rubin DB. Maximum likelihood from incomplete data via the EM algorithm. J Royal Statistical Soc Ser B Methodol 1977;39(1):1–38.

Please cite this article in press as: Zeraatkar N, et al., Resolution-recovery-embedded image reconstruction for a high-resolution animal SPECT system, Physica Medica (2014), http://dx.doi.org/10.1016/j.ejmp.2014.05.013

[14] Hudson HM, Larkin RS. Accelerated image-reconstruction using ordered subsets of projection data. IEEE Trans Med Imaging 1994;13(4):601–9.
[15] Frey EC, Tsui BMW. Collimator-detector response compensation in SPECT. In: Zaidi H, editor. Quantitative analysis in nuclear medicine imaging. Singapore: Springer; 2006. pp. 141–66.
[16] Rahmim A, Zaidi H. PET versus SPECT: strengths, limitations and challenges. Nucl Med Commun 2008;29(3):193–207.
[17] Zeng GSL, Gullberg GT, Bai CY, Christian PE, Trisjono F, Di Bella EVR, et al. Iterative reconstruction of fluorine-18 SPECT using geometric point response correction. J Nucl Med 1998;39(1):124–30.
[18] Bouwens LR, Gifford H, Van de Walle R, King MA, Lemahieu I, Dierckx RA. Resolution recovery for list-mode reconstruction in SPECT. P Soc Photo-Opt Ins 2001;2(27):40–51.
[19] Yao RT, Ma TY, Shao YP. Derivation of system matrix from simulation data for an animal SPECT with slit-slat collimator. IEEE Trans Nucl Sci 2009;56(5): 2651–8.
[20] Tsui BM, Hu HB, Gilland DR. Implementation of simultaneous attenuation and detector response correction in SPECT. IEEE Trans Nucl Sci 1988;35: 778–83.
[21] Sajedi S, Zeraatkar N, Moji V, Farahani MH, Sarkar S, Arabi H, et al. Design and development of a high resolution animal SPECT scanner dedicated for rat and mouse imaging. Nuclear instruments and methods in physics research section A: accelerators, spectrometers. Detect Assoc Equip 2014;741:169–76.
[22] McCarthy AW, Miller MI. Maximum likelihood SPECT in clinical computation times using mesh-connected parallel computers. IEEE Trans Med Imaging 1991;10(3):426–36.
[23] Zeng GL, Gullberg GT. Frequency-domain implementation of the 3-dimensional geometric point response correction in spect imaging. IEEE Trans Nucl Sci 1992;39(5):1444–53.
[24] Di Bella EVR, Barclay AB, Eisner RL, Schafer RW. A comparison of rotation-based methods for iterative reconstruction algorithm. IEEE Trans Nucl Sci 1996;43(6):3370–6.
[25] Shepp LA, Logan BF. The fourier reconstruction of a head section. IEEE Trans Nucl Sci 1974;21(3):21–43.
[26] Rahmim A, Cheng JC, Dinelle K, Shilov M, Segars WP, Rousset OG, et al. System matrix modelling of externally tracked motion. Nucl Med Commun 2008;29(6):574–81.
[27] Association NEM. Performance measurements of small animal positron emission tomographs. NU 4–2008. NEMA Standards Publication; 2008.
[28] Rahmim A, Qi J, Sossi V. Resolution modeling in PET imaging: theory, practice, benefits, and pitfalls. Med Phys 2013;40(6). 064301.
[29] Rahmim A, Tang J. Noise propagation in resolution modeled PET imaging and its impact on detectability. Phys Med biology 2013;58:6945–68.
[30] Rodríguez-Villafuerte M, Yang Y, Cherry S. A Monte Carlo investigation of the spatial resolution performance of a small-animal PET scanner designed for mouse brain imaging studies. Phys Medica 2014;30(1):76–85.

Please cite this article in press as: Zeraatkar N, et al., Resolution-recovery-embedded image reconstruction for a high-resolution animal SPECT system, Physica Medica (2014), http://dx.doi.org/10.1016/j.ejmp.2014.05.013